Design Modeling and Sizing Equations of V-shape IPM Motors

A. Di Gerlando, C. Ricca

Abstract – **The paper develops the model of a V-shape IPM motor for automotive applications. The approach, design oriented, considers saturation and cross-coupling, by suited saturation factors. A torque sizing equation is obtained, independent on the winding data, and the main constructional data are gained, considering the corner operating point. Then the detailed motor design is completed, and the calculation of the torque-speed curve is extended also in the flux-weakening zone. FEM analysis validates the model.**

Index Terms—**IPM motors, cross saturation, saturation functions, magnetic circuits, sizing equations, analytical design, flux weakening, inductance calculation, variable speed drive.**

I. Introduction

THE IPM motor is widely popular in automotive applications, thanks to a few positive features: high torque density and efficiency, wide flux weakening region extension, simple stator structure and compact rotor layout. However, its model is not simple, for several reasons: critical rotor bridges sizing; highly saturated operating conditions, with significant cross-coupling; cogging and torque ripple.

During the last years, significant efforts have been devoted to improving the IPM motor model.

Most of the papers are aimed to develop accurate models for the motor operation analysis: in [1], some equivalent magnetic circuits are settled, valid for no-load operation; [2] compares some rotor topologies, by considering phasor diagrams; [3]-[8] analyze air-gap flux density distributions, develop equivalent magnetic circuits, and identify d-q flux-current links and inductance curves, by FEM analysis.

Other papers are focused on control aspects: d-q flux-current curve linearization [9], rotor layout analysis and FEM parameter identification for sensorless control [10].

Some papers are oriented to the motor design, sometimes with analytical approach [11]-[13]; in other cases, optimization methods are developed, based on FEM [14].

Moreover, a few commercial software tools (Speed®, Ansys MotorCad®, Ansys Rmxprt®) developed the motor design: however, usually input data are motor dimensions, while no sizing equations are offered, to start the procedure.

This paper develops an IPM motor sizing procedure, implemented in MathCad®, based on a torque sizing equation: it includes saturation and cross-coupling effects by suited pu saturation factors. Section II defines the motor layout, and some basic quantities. Section III develops the q-axis saturation model. Section IV defines the rotor bridges and gains the PM flux cross-coupling saturation function. Section V develops the sizing torque function and finds the optimal phase advance. Section VI obtains winding and core data. Section VII calculates reaction factors and electrical parameters. Section VIII presents performance calculations in the full operating range, and compares results with FEM.

A. Di Gerlando and C. Ricca are with Politecnico di Milano, Department of Energy, Via La Masa 34, 20156 Milano, Italy, antonino.digerlando@polimi.it, claudio.ricca@polimi.it

II. IPM Motor Layout and Basic Data

Fig. 1 shows the IPM motor layout, with the main dimensions, and Table I reports some motor basic data.

Some comments are suitable:

- the choice of stator diameter D and air-gap width g leads to calculate other design quantities directly and accurately;
- a 2-layer winding, with q = 5/2, limits cogging and torque ripple; with coil pitch y_c = 6, the winding factor is k_w= 0.91;
- the last row of Table I reports iterative quantities, defined later and updated during the design process: here the final values are given, reached in one or two iterations.

III. q-axis Saturation Model

The $H_{fe}(B_{fe})$ lamination magnetization curve, provided by the manufacturer, is suitably extended to high B_{fe} values, in such a way that the end incremental permeability tends to μ_0.

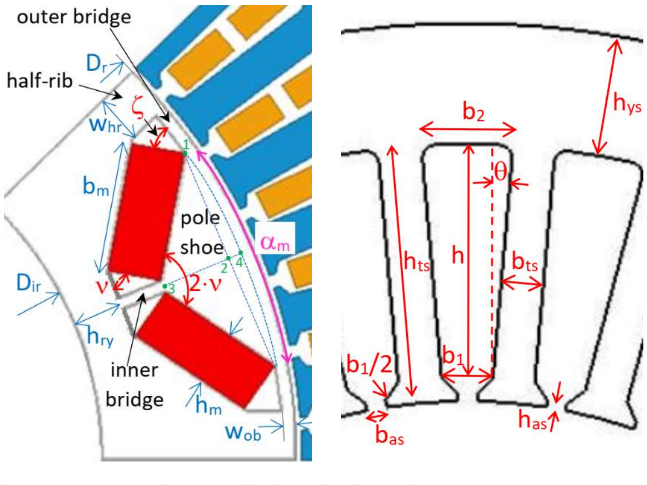

Fig. 1. IPM motor layout, with the main dimensions.

TABLE I
Main Specifications, Used materials, Basic Data

Corner point: torque T_c [Nm]; speed N_c [RPM]	200; 2900
Max. speed N_M [RPM]; DC link V: V_{dc} [V]	13500; 650
Materials: stator and rotor laminations; PM	M235-35A; N48UZ-SGR
PM param.: $B_{r20°C}$ [T]; μ_{rec} [pu]; k_{Br} [%/°C]	1.37; 1.05; –0.1
Winding ref. temper.; PM ref. temper. [°C]	180; 140
Stator bore D; air-gap g; slot open. b_{as} [mm]	160; 1; 2
Phases; poles No: p; slots/(pole·phase) No: q	3; 8; 5/2
Parameters: $\rho_{bt.\tau s}$; $\rho_{hte.g}$; $\sigma_{anis.o}$; c_d ; ρ_{EV}	0.704; 52.4; 4.11; 0.201; 0.65

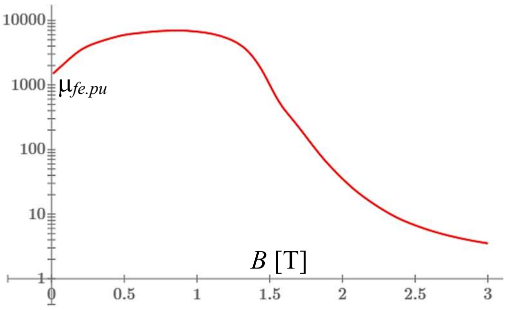

Fig. 2. Extended curve of pu permeability of M235-35A lamination.

The corresponding pu apparent permeability curve $\mu_{fe.pu}(B_{fe})$, from (1), is shown in fig. 2: depending on the equations to be managed, $H_{fe}(B_{fe})$ or $\mu_{fe.pu}(B_{fe})$ will be used.

$$\mu_{fe.pu}\left(B_{fe}\right)=B_{fe}\Big/\left[\mu_0\cdot H_{fe}\left(B_{fe}\right)\right] \tag{1}$$

In the next sections, the following function will be used:

$$y\left(x\right)=root\left(f\left(x,y_G\right),y_G\right)\ : \tag{2}$$

y_G is a guess value of y, that satisfies the condition: $f(x, y)=0$.

A first case of (2) is (3), that gives the peak flux density B_t in the q-axis aligned tooth as a function of the air-gap peak flux density B_{gI}, due to the q-axis reaction current I only:

$$B_t\left(B_{gI}\right)=root\left(B_{tG}-\frac{B_{gI}}{\rho_{bt.\tau s}\cdot k_{st}}+\frac{\mu_0\cdot H_{fe}\left(B_{tG}\right)}{k_{st}}\cdot\left(\frac{1}{\rho_{bt.\tau s}}-1\right),B_{tG}\right). \tag{3}$$

(3) follows from the equality between the pole air-gap flux and the sum of the flux in the teeth in one pole and in the slots in one pole, in parallel with the teeth; $\rho_{bt.\tau s}=b_t/\tau_s$ is the tooth width over tooth pitch ratio, $k_{st}=0.97$= stacking factor.

Assuming that the magnetic voltage drop (MVD) in the teeth U_t is the main ferromagnetic voltage drop contribution, the saturation ratio function, due to q-axis reaction, equals:

$$\rho_{sat}\left(B_{gI}\right)=\frac{U_g+U_t}{U_g}=1+\frac{H_{fe}\left(B_t\left(B_{gI}\right)\right)\cdot\rho_{hte.g}}{B_{gI}\cdot\mu_0^{-1}\cdot k_C}. \tag{4}$$

$\rho_{hte.g}=h_{te}/g$ is the tooth heigth over air-gap width ratio; k_C = 1.071 is the Carter's factor, function of $\tau_s=(\pi D)/(3pq)$, b_{as}, g. (4) leads to obtain the peak stator MMF M_I (acting along q axis), able to give the peak flux density B_{gI} in the air-gap, by (5), and its inverse function, (6) (with ρ used instead of gI):

$$M_I\left(B_{gI}\right)=\left(B_{gI}/\mu_0\right)\cdot g\cdot k_C\cdot\rho_{sat}\left(B_{gI}\right) \tag{5}$$

$$B_\rho\left(M_{\rho q}\right)=root\left(M_I\left(B_{gIG}\right)-M_{\rho q},B_{gIG}\right)\quad, \tag{6}$$

where $M_{\rho q}$ is the q axis reaction MMF.

Finally, the saturation factor σ_{sM} can be defined as follows:

$$\sigma_{sM}\left(M_{\rho q}\right)=B_\rho\left(M_{\rho q}\right)\Big/\left[\mu_0\cdot M_{\rho q}/\left(g\cdot k_C\right)\right] \tag{7}$$

Fig. 3 shows the saturation factor curve: it should be observed that the shape of σ_{sM} for small $M_{\rho q}$ values is similar to the initial behavior of the curve $\mu_{fe.pu}(B_{fe})$ in fig. 2.

IV. Rotor Bridges Sizing and Check and PM Flux Saturation Factor

Fig. 4 shows the field map of the IPM motor under no-load conditions, for the following design parameters (fig. 1):

h_m = 6mm; ν = 78 deg; w_{ob} = 0.5mm; w_{ib} = 2.5mm; $w_{hr}=0.55\cdot\tau_s$ = 4.6mm; $h_{ry}=1.5\cdot w_{hr}$ = 6.9mm; α_m = 0.754 pu.

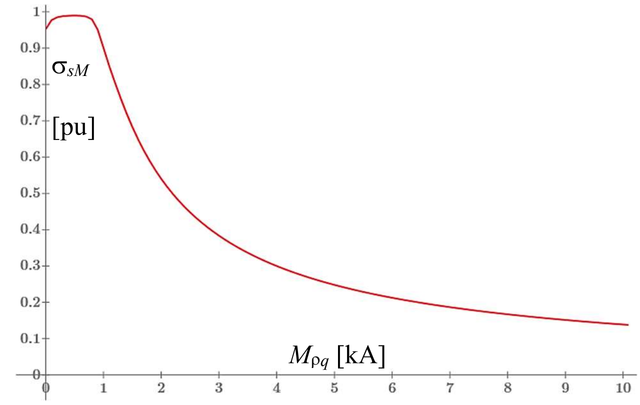

Fig. 3. Saturation factor as a function of the peak q-axis MMF $M_{\rho q}$.

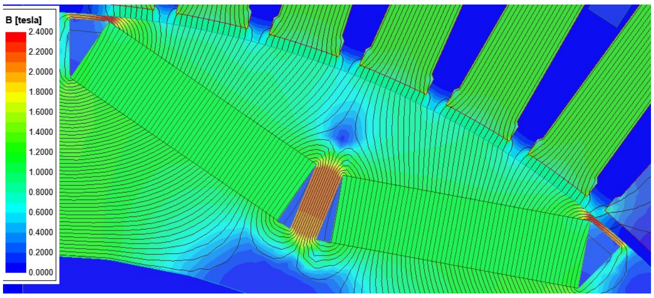

Fig. 4. Field map of the IPM motor, under no-load operating conditions.

Assuming these data, the other rotor sizes are defined by the following equations (where $\tau=\pi\cdot D/p$ is the pole pitch):

pole shoe extension: $$b_{ps}=\alpha_m\cdot\tau_r=\alpha_m\cdot\tau\cdot D_r/D \tag{8}$$

outer bridge length: $$h_{ob}=\left(\tau_r-2\cdot w_{hr}-b_{ps}\right)\Big/2=3\text{mm} \tag{9}$$

side PM angle: $$\zeta=acos\left[\left(h_{ob}\cdot\left(D_r-2\cdot w_{ob}\right)\cdot D_r^{-1}\right)\Big/h_m\right] \tag{10}$$

inner bridge length: $$h_{ib}=h_m\cdot sin\left(\nu\right)=5.9\text{mm} \tag{11}$$

half rib radial length: $$h_{hr}=h_m\cdot sin\left(\zeta\right)=5.2\text{mm} \tag{12}$$

length d_{12} (fig. 1): $$d_{12}=\left(D_r/2-w_{ob}\right)\cdot sin\left(\alpha_m\cdot\pi/p\right) \tag{13}$$

length d_{23}: $$d_{23}=\left(d_{12}-w_{ib}/2\right)\cdot\left[tan\left(\nu\right)\right]^{-1} \tag{14}$$

length d_{24}: $$d_{24}=\left(D_r/2-w_{ob}\right)-d_{12}\cdot\left[tan\left(\alpha_m\cdot\pi/p\right)\right]^{-1} \tag{15}$$

pole shoe radial depth: $$d_{ps}=d_{23}+d_{24}+w_{ob}=8.5\text{mm} \tag{16}$$

int. rotor ∅: $$D_{ir}=D_r-2\cdot\left(d_{ps}+h_{ib}+h_{ry}\right)=115.4\text{mm} \tag{17}$$

PM segment width: $$b_m=\left(d_{12}-w_{ib}/2\right)\Big/sin\left(\nu\right)=22.1\text{mm} \tag{18}$$

As concerns the width of the bridges, $w_{ib}=5\cdot w_{ob}$ occurs: in fact, w_{ob} is sized at the minimum value (respecting the practical rule $w_{ob}>w_{lam}$ = 0.35mm), while the centrifugal force f_{max} at the maximum speed, due to the mass m_{1p} of pole shoe and PM segments, is sustained by the inner bridge:

specific max centrifugal force: $$f_{max}=m_{1p}\cdot R_{av}\cdot\Omega_{max}^2 \tag{19}$$

ideal stress of the inner bridge: $$\sigma_{ib.i}=f_{max}\Big/\left(w_{ib}\cdot k_{st}\right) \tag{20}$$

actual stress (K_t=1.66: concentration factor): $$\sigma_{ib}=K_t\sigma_{ib.i} \tag{21}$$

(bridge stress)/(lam. yield strength): $$\sigma_{ib}\big/\sigma_{y.lam}=0.783\,. \tag{22}$$

The analysis of the cross coupling effect of the q-axis reaction MMF on the air-gap flux delivered by the PM can be based on the equivalent magnetic network of fig. 5.

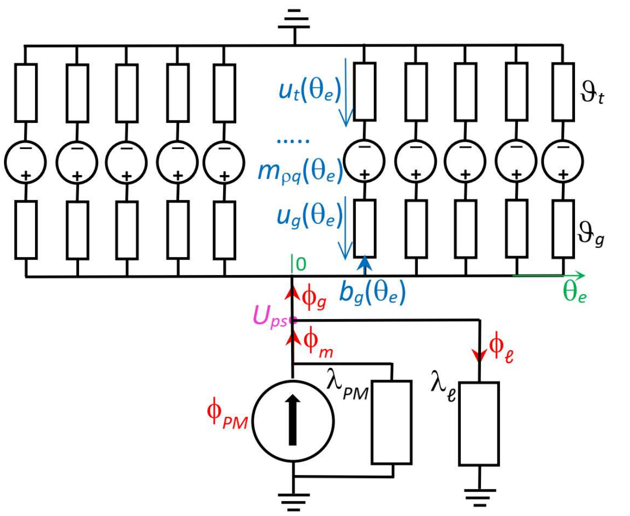

Fig. 5. Per-pole magnetic network for the analysis of the cross coupling effect of the q-axis reaction MMF on the air-gap flux delivered by the PM.

The network, for unity length in axial direction, consists of a concentrated parameter rotor sub-network (bottom part), and of a distributed parameter sub-network (top part), modeling the distributed toothed portion and MMF. The pole shoe, that connects the two sub-networks, has a scalar magnetic potential equal to U_{ps}, unknown. The equations are:

q-axis MMF distribution $m_{\rho q}\left(\theta_e, M_{\rho q}\right) = M_{\rho q} \cdot sin\left(\theta_e\right)$ (23)

PM residual specific flux: $\phi_{PM} = B_r \cdot 2 \cdot b_m$ (24)

PM specific permeance: $\lambda_{PM} = \mu_{rec.pu} \cdot \mu_0 \cdot 2 \cdot b_m \cdot h_m^{-1}$ (25)

inner bridge MVD: $U_{ib}\left(B_{ib}\right) = h_{ib} \cdot B_{ib} \Big/ \left(\mu_0 \cdot \mu_{fe.pu}\left(B_{ib}\right)\right)$ (26)

outer bridge MVD: $U_{ob}\left(B_{ob}\right) = h_{ob} \cdot B_{ob} \Big/ \left(\mu_0 \cdot \mu_{fe.pu}\left(B_{ob}\right)\right)$ (27)

outer br. flux density: $B_{ob}\left(U\right) = root\left[U_{ob}\left(B_{bG}\right) - U, B_{bG}\right]$ (28)

inner br. flux density: $B_{ib}\left(U\right) = root\left[U_{ib}\left(B_{bG}\right) - U, B_{bG}\right]$ (29)

leakage flux: $\phi_\ell\left(U_{ps}\right) = B_{ib}\left(U_{ps}\right) k_{st} w_{ib} + 2 B_{ob}\left(U_{ps}\right) k_{st} w_{ob}$ (30)

air-gap specific flux, as delivered by the rotor:

$$\phi_{gr}\left(U_{ps}\right) = \phi_{PM} - \lambda_{PM} \cdot U_{ps} - \phi_\ell\left(U_{ps}\right) \quad (31)$$

air-gap MVD distribution (with U_{ps} unknown):

$$u_g\left(\theta_e, M_{\rho q}, U_{ps}, b_{gL}\right) = U_{ps} - M_{\rho q} sin\left(\theta_e\right) - H_{fe}\left(B_t\left(b_{gL}\right)\right) \cdot \rho_{hte.g} \cdot g \quad (32)$$

air-gap flux density distribution b_{gU} (with U_{ps} unknown):

$$b_{gU}\left(\theta_e, M_{\rho q}, U_{ps}\right) = root\left(b_{gUG} - \mu_0 \frac{u_g\left(\theta_e, M_{\rho q}, U_{ps}, b_{gUG}\right)}{g \cdot k_C}, b_{gUG}\right) \quad (33)$$

air-gap specific flux, as received by the stator:

$$\phi_{gs}\left(U_{ps}, M_{\rho q}\right) = \frac{2}{p} \cdot \frac{D}{2} \cdot \int_{-\alpha_m \cdot \pi/2}^{\alpha_m \cdot \pi/2} b_{gU}\left(\theta_e, M_{\rho q}, U_{ps}\right) \cdot d\theta_e \quad (34)$$

pole shoe potential, as a function of the reaction MMF $M_{\rho q}$:

$$U_{ps\rho}\left(M_{\rho q}\right) = root\left[\phi_{gr}\left(U_{ps\rho G}\right) - \phi_{gs}\left(U_{ps\rho G}, M_{\rho q}\right), U_{ps\rho G}\right] \quad (35)$$

flux density distribution in the air-gap, as a function of $M_{\rho q}$:

$$b_g\left(\theta_e, M_{\rho q}\right) = b_{gU}\left[\theta_e, M_{\rho q}, U_{ps\rho}\left(M_{\rho q}\right)\right] . \quad (36)$$

In fig. 6, (35) and (36) are shown; it can be observed that:

– the pole shoe potential highly changes with $M_{\rho q}$ increase;

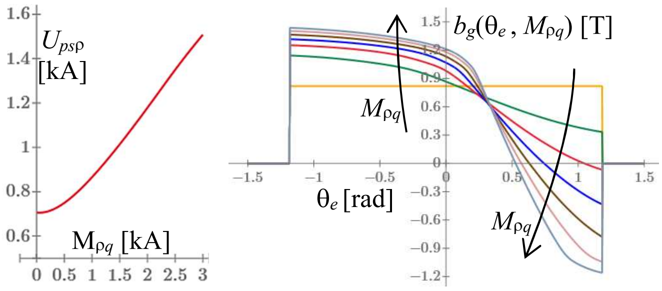

Fig. 6. Left: pole shoe potential as a function of $M_{\rho q}$; right: air-gap flux density distribution ($M_{\rho q}$ parameter); $M_{\rho q}$ values: 0, 0.5, 1, 1.5, 2, 2.5, 3 kA.

– the flux density distribution b_g is distorted if $M_{\rho q}$ rises;

– moreover, due to local teeth saturation, the b_g increase on the left is lower than the b_g decrease on the right.

By integrating $b_g(\theta_e, M_{\rho q})$ within the pole shoe extension ($|\theta_e| < \alpha_m \cdot \pi/2$) gives the specific air-gap flux, due to PM:

$$\phi_g\left(M_{\rho q}\right) = \phi_{gr}\left(U_{ps\rho}\left(M_{\rho q}\right)\right) \quad (37)$$

It is useful to introduce the PM flux saturation factor:

$$\eta_{\phi M}\left(M_{\rho q}\right) = \phi_g\left(M_{\rho q}\right) \Big/ \phi_g\left(0\right) , \quad (38)$$

whose dependence on $M_{\rho q}$ is shown in fig. 7.

In (38) $\phi_g(0) = \phi_{go}$ is the specific air gap flux within the pole shoe extension, due to PMs, with zero $M_{\rho q}$, corresponding to the flat flux density yellow distribution in fig. 6 right:

$$\phi_{go} = \phi_g(0) = 38.801 \text{ mWb/m} . \quad (39)$$

Another diagram of interest is the leakage ratio ϕ_e/ϕ_m between the leakage flux in the bridges and the PM flux, shown in fig. 8: it gives information about the magnetic effect of the bridges sizing. As can be seen, in no-load conditions the leakage ratio equals 16.6%, that is acceptable; however it increases significantly at the increase of $M_{\rho q}$.

The no-load flux density B_{go} of the $b_g(\theta_e,0)$ distribution is:

$$B_{go} = \phi_{go} \big/ \left(\alpha_m \cdot \tau\right) = 0.819 \text{ T} \quad \text{(iterative result)}, \quad (40)$$

while its fundamental component equals:

$$B_{g1o} = \frac{4}{\pi} \cdot \int_0^{\alpha_m \cdot \pi/2} B_{go} \cdot cos\left(\theta_e\right) \cdot d\theta_e = \frac{4}{\pi} sin\left(\alpha_m \frac{\pi}{2}\right) \cdot B_{go} = 0.965 \text{ T} \quad (41)$$

The no-load specific fundamental flux is given by:

$$\phi_{g1o} = \left(2/\pi\right) \cdot B_{g1o} \cdot \tau = 38.616 \text{ mWb/m} . \quad (42)$$

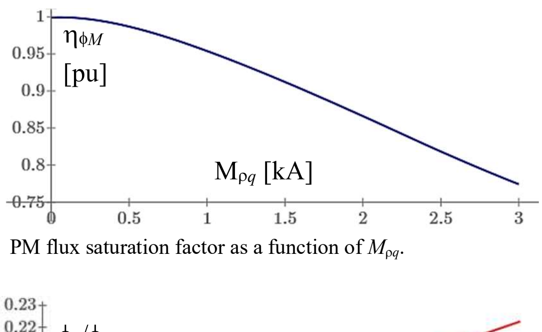

Fig. 7. PM flux saturation factor as a function of $M_{\rho q}$.

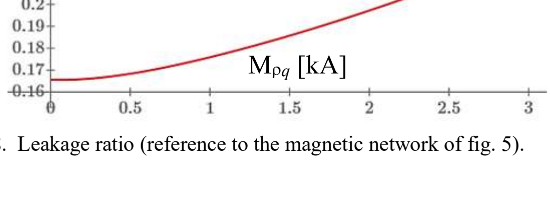

Fig. 8. Leakage ratio (reference to the magnetic network of fig. 5).

Finally, it is assumed that the fundamental air-gap flux due to the PM, as a function of $M_{\rho q}$, can be calculated as follows:

$$\phi_{g1}\left(M_{\rho q}\right)=\phi_{g1o}\cdot\eta_{\phi M}\left(M_{\rho q}\right) \quad . \tag{43}$$

V. Torque Function

As well known, the phasor diagram of fig. 9 leads to obtain the expression (44) of the electromagnetic torque:

$$T=3\cdot\frac{p}{2}\cdot\left[\Psi_{PM1}\cdot I_q-\left(L_q-L_d\right)\cdot I_d\cdot I_q\right] \quad . \tag{44}$$

Considering that the winding data are unknown at this stage, all the quantities should be given in terms of loadings: air-gap flux density B_{g1} and linear current density Δ.

So, the reaction MMF M_ρ, the saturation functions σ_{sM}, $\eta_{\phi M}$, and the PM flux linkage Ψ_{PM1} should be rewritten as follows:

$$M_\rho=k_M\cdot I=\frac{3\cdot\sqrt{2}}{\pi}\cdot\frac{k_w\cdot U_c}{p}\cdot I=\frac{\sqrt{2}}{\pi}\cdot k_w\cdot\tau\cdot\Delta \tag{45}$$

$$\sigma_s\left(\Delta,\gamma\right)=\sigma_{sM}\left(\left(\sqrt{2}/\pi\right)\cdot k_w\cdot\tau\cdot\Delta\cdot cos\left(\gamma\right)\right) \tag{46}$$

$$\eta_\phi\left(\Delta,\gamma\right)=\eta_{\phi M}\left(\left(\sqrt{2}/\pi\right)\cdot k_w\cdot\tau\cdot\Delta\cdot cos\left(\gamma\right)\right) \tag{47}$$

$$\Psi_{PM1}=\Psi_{PMo1}\cdot\eta_\phi\left(\Delta,\gamma\right)=k_w\cdot U_c\cdot\frac{\phi_{g1o}\cdot\eta_\phi\left(\Delta,\gamma\right)}{2\cdot\sqrt{2}}\cdot\ell \quad . \tag{48}$$

with U_c = phase series connected conductors. The L_q-L_d difference equals the reaction inductance difference:

$$L_q-L_d=L_{\rho q}-L_{\rho d} \tag{49}$$

In case of isotropic rotor and unsaturated motor, the reaction inductance is given by (50), with λ_{is} specific permeance:

$$L_{\rho.is}=\left(U_c^2/p\right)\cdot\lambda_{is}\cdot\ell \tag{50}$$

$$\lambda_{is}=\mu_0\cdot k_w^2\cdot\left(3/\pi^2\right)\cdot\tau/\left(g\cdot k_C\right)=15.543\ \mu\text{H/m} \quad . \tag{51}$$

The unsaturated reaction inductances are expressed as:

$$L_{\rho do}=c_d\cdot L_{\rho.is} \quad , \qquad L_{\rho qo}=c_q\cdot L_{\rho.is} \quad , \tag{52}$$

with c_q, c_d reaction factors: their ratio is the anisotropy ratio:

$$\sigma_{an.o}=L_{\rho qo}/L_{\rho do}=c_q/c_d \quad . \tag{53}$$

In the following, the d-axis reaction inductance $L_{\rho d}$ will be considered as unsaturated:

$$L_{\rho d}=L_{\rho do} \quad . \tag{54}$$

The reason for this model approximation, acceptable for a practical design approach, is the high d-axis equivalent air-gap ($g_{d.eq}=g\cdot k_C+h_m/\mu_{rec}$), that linearizes the $\Psi_{\rho d}$ - I_d curve.

In contrast, the q-axis reaction inductance is saturated, because of the small equivalent air-gap ($g_{q.eq}=g\cdot k_C$):

$$L_{\rho q}=L_{\rho qo}\cdot\sigma_s\left(\Delta,\gamma\right) \quad . \tag{55}$$

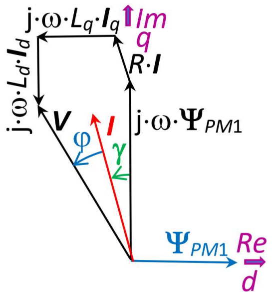

Fig. 9. Phasor diagram of the IPM motor.

Thus, the inductance difference $L_{\rho q}$–$L_{\rho d}$ can be written as:

$$L_{\rho q}-L_{\rho d}=L_{\rho do}\cdot\left(\sigma_{an.o}\cdot\sigma_s\left(\Delta,\gamma\right)-1\right) \quad . \tag{56}$$

By considering (44) (in which $I_d<0$), (48) and (56), it is useful to introduce the following pu torque function $f_T(\Delta,\gamma)$:

$$f_T\left(\Delta,\gamma\right)=f_{T.al}\left(\Delta,\gamma\right)+f_{T.an}\left(\Delta,\gamma\right)=\eta_\phi\left(\Delta,\gamma\right)cos\left(\gamma\right)+$$
$$+\frac{\sqrt{2}\pi}{6}\cdot\frac{c_d\lambda_{is}}{k_w B_{g1o}}\cdot\Delta\cdot\left(\sigma_{an.o}\cdot\sigma_s\left(\Delta,\gamma\right)-1\right)\cdot sin\left(2\gamma\right) \quad . \tag{57}$$

$f_T(\Delta,\gamma)$ consists of an alignment term, $f_{T.al}$, and of an anisotropy term, $f_{T.an}$: fig. 10 shows $f_T(\Delta,\gamma)$ as a function of γ, with parameter Δ. As can be observed, for any Δ value, a value of γ exists for which $f_T(\Delta,\gamma)$ shows a maximum. Thus, (58) allows to obtain the optimum phase advance γ_{opt} as a function of the linear current density Δ, as shown in fig. 11:

$$\gamma_{opt}\left(\Delta\right)=root\left(df_T\left(\Delta,\gamma_{optG}\right)/d\gamma_{optG},\gamma_{optG}\right) . \tag{58}$$

From (44), the optimal specific torque (for unity length in axial direction) can be written as:

$$T_\ell\left(\Delta\right)=f_T\left(\Delta,\gamma_{opt}\left(\Delta\right)\right)\cdot\frac{\pi\cdot k_w}{2\cdot\sqrt{2}}\cdot B_{g1o}\cdot\Delta\cdot D^2 \quad , \tag{59}$$

and its trend is shown in fig. 12.

A few comments:

– T_ℓ always increases for increasing Δ values, even if beyond 75 kA/m the $T_\ell(\Delta)$ slope slightly decreases, corresponding to the trend of maximum values in fig. 10;

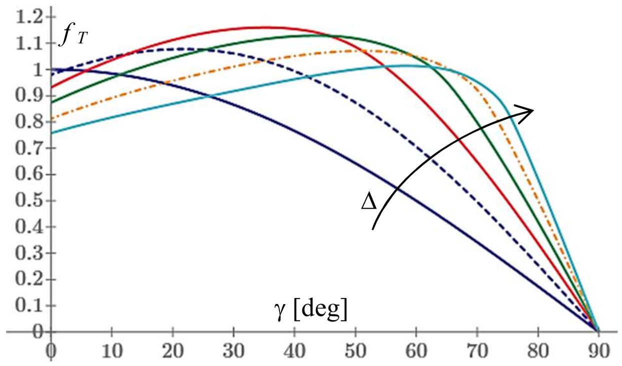

Fig. 10. Torque function (57), for Δ values: Δ=0, 25, 50, 75, 100, 125 kA/m.

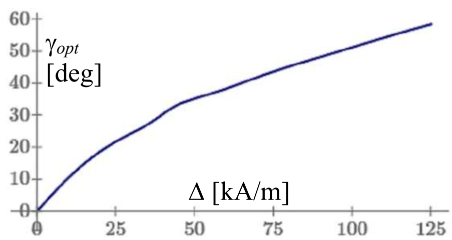

Fig. 11. Optimal phase advance, as a function of the linear current density.

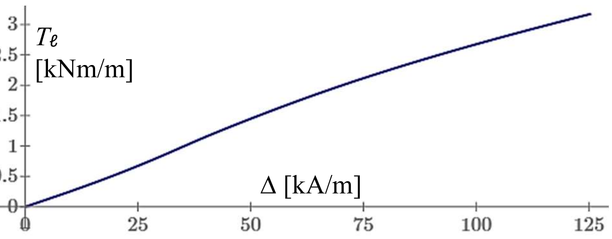

Fig. 12. Optimal specific torque, as a function of the linear current density.

– the choice of Δ mainly depends on thermal considerations (steady-state or short-term thermal conditions).

Δ_c = 90 kA/m will be adopted for the corner point (a water-glycol cooling system is supposed); it implies:

$$\gamma_{opt.c} = \gamma_{opt}(\Delta_c) = 48.15 \text{ deg}, \quad (60)$$

and the following values occur:

$$\eta_{\phi c} = \eta_\phi\left(\Delta_c, \gamma_{opt.c}\right) = 0.909 \quad (61)$$

$$\sigma_{sc} = \sigma_s\left(\Delta_c, \gamma_{opt.c}\right) = 0.667 \quad (62)$$

$$T_{\ell c} = T_\ell\left(\Delta_c\right) = 2.461 \text{ kNm/m} . \quad (63)$$

Thus, the needed lamination stack length ℓ equals:

$$\ell = T_c / T_{\ell c} = 81.3 \text{ mm} . \quad (64)$$

VI. Winding Data and Stator Core Dimensions

In the following, the detailed stator design is defined:

fundam. pole flux: $\Phi_{g1c} = \eta_{\phi c} \cdot \phi_{g1o} \cdot \ell = 2.853$ mWb (65)

conductor EMF: $E_{cc} = \left(\pi/\sqrt{2}\right) \cdot f_c \cdot \Phi_{g1c} = 1.225\ \mathrm{V_{rms}}$ (66)

EMF over Voltage ratio (iterative result): $\rho_{EV} = 0.650$ (67)

max. inverter phase voltage $V_{invM} = 0.95 \cdot V_{dc} / \left(2\sqrt{2}\right)$ (68)

conductors in series: $U_{c.th} = \left(\rho_{EV} V_{invM}\right) / \left(k_w E_{cc}\right) = 127.30$ (69)

parallel paths: $a = p/2 = 4$ (70)

conductors in slot (theor.) $u_{th} = \left(3 \cdot U_{c.th} \cdot a\right) / N_s = 25.46$ (71)

actual conductors in slot: $u = 2 \cdot round\left(0.5 \cdot u_{th}\right) = 26$ (72)

actual conductors in series: $U_c = \left(N_s \cdot u\right) / \left(3 \cdot a\right) = 130$ (73)

phase EMF: $E_c = E_{cc} \cdot U \cdot k_w = 144.9\ \mathrm{V_{rms}}$ (74)

phase current: $I_c = \left(\Delta_c \cdot p \cdot \tau\right) / \left(3 \cdot U\right) = 116\ \mathrm{A_{rms}}$ (75)

path current: $I_{c.path} = I_c / a$ (76)

theoretical current density: $S_{cth} = 8\ \mathrm{A/mm^2}$ (77)

conductor cross section: $A_u = I_{c.path} / S_{cth} = 3.625\ \mathrm{mm^2}$ (78)

max wire diameter: $d_{wmax} = b_{as} - d_{clearance}$ (79)

strands in hand: $n_w = ceil\left(\left(4/\pi\right) \cdot A_u / d_{wmax}^2\right) = 8$ (80)

wire diameter: $d_{wcu} \approx \sqrt{\left(4/\pi\right) \cdot \left(A_u / n_w\right)} = 0.75$ mm (81)

copper cross section in slot: $A_{cu.slot} = u \cdot n_w \cdot \left(\pi/4\right) \cdot d_{wcu}^2$ (82)

copper filling factor in slot: $\alpha_{cu} = 0.4$ (83)

slot cross section: $A_{slot} = A_{cu.slot} / \alpha_{cu}$ (84)

tooth width: $b_{ts} = \left(B_{g1o} / B_{ts}\right) \cdot \tau_s / k_{st} = 5.89$ mm (85)

$\rho_{bt.\tau s}$ ratio: $\rho_{bt.\tau s} = b_{ts} / \tau_s = 0.704$ (iterative result) (86)

minor slot width: $b_1 = \left[\pi \cdot \left(D + 2 \cdot h_{as}\right) - N_s \cdot b_{ts}\right] / \left(N_s - \pi\right)$ (87)

auxiliary slot parameter: $k_\theta = tan\left(\theta\right) = tan\left(\pi / N_s\right)$ (88)

slot height: $h = \left(-b_1 + \sqrt{b_1^2 + 2k_\theta \cdot \left(2A_{slot} - b_1^2 \cdot \pi/4\right)}\right) / \left(2k_\theta\right)$ (89)

total tooth equivalent height: $h_{teq} = h + b_1/2 + h_{as} + h_{hr}$ (90)

ratio $\rho_{hte.g}$ (iterative result): $h_{teq} / g = 52.44$ (91)

major slot width: $b_2 = b_1 + 2 \cdot h \cdot k_\theta = 7.44$ mm (92)

stator yoke width: $h_{sy} = \phi_{g1o} / \left(2 \cdot B_{ys} \cdot k_{st}\right) = 20.0$ mm (93)

ext. stator $\varnothing$: $D_{es} = D + 2 \cdot \left(h_{as} + h_{ts} + h_{sy}\right) = 294.5$ mm . (94)

Eq. (90) shows that the equivalent tooth height is higher than the stator tooth height: in fact, it includes the rotor rib height, saturated by $M_{\rho q}$ roughly in the same way of the stator teeth.

VII. Electrical Parameters

The peak reaction flux densities with isotropic rotor are:

$$B_{\rho d.is} = \mu_0 \cdot M_{\rho d} / \left(k_C \cdot g\right) \;,\; B_{\rho q.is} = \mu_0 \cdot M_{\rho q} / \left(k_C \cdot g\right) . \quad (95)$$

In the following, the reaction coefficients c_d, c_q are obtained: they are defined assuming unsaturated conditions (apart from the bridges, that are considered as consisting of air, because completely saturated by the PM leakage fluxes).

A. *d-axis reaction*

The air-gap MVD due to d-axis reaction equals:

$$u_{gd}\left(\theta_e\right) = M_{\rho d} \cdot cos\left(\theta_e\right) - U_{ps\rho d} \;, \text{ where} \quad (96)$$

$$M_{\rho d} = \left(3 \cdot \sqrt{2}/\pi\right) \cdot \left(k_w \cdot U_c / p\right) \cdot I_d \quad \text{and} \quad (97)$$

$U_{ps\rho d}$ is the d-axis reaction pole shoe potential (unknown). The distribution of d-axis reaction flux density in the air-gap is expressed as follows:

$$b_{\rho d}\left(\theta_e\right) = \begin{cases} \mu_0 \cdot u_{gd}\left(\theta_e\right) / \left(k_C \cdot g\right) \;, & 0 < \theta_e < \alpha_m \pi/2 \\ 0 \;, \; \alpha_m \frac{\pi}{2} < \theta_e < \theta_{e.rib} = \alpha_m \frac{\pi}{2} + \frac{p}{2} \frac{h_{ob}}{D_r/2} & \\ B_{\rho d.is} \cdot cos\left(\theta_e\right) \;, & \theta_{e.rib} < \theta_e < \pi/2 \end{cases} \quad (98)$$

The radial permeance of the rotor internal V-shape holes is:

$$\Lambda_{ps.ir} = \mu_0 \cdot \ell \cdot \left(2 \cdot b_m + h_m \cdot cos\left(\nu\right) + w_{ib}\right) / h_m \;, \quad (99)$$

and the North flux from inner rotor part to the pole shoe is:

$$\Phi_{ps.ir} = \Lambda_{ps.ir} \cdot U_{ps\rho d} \;. \quad (100)$$

The flux delivered by the pole shoe to the air-gap is given by:

$$\Phi_{ps.g} = 2\ell \cdot \int_0^{\alpha_m \cdot \tau/2} \mu_0 \cdot \frac{M_{\rho d} \cdot cos\left(\pi \cdot x/\tau\right) - U_{ps\rho d}}{k_C \cdot g} \cdot dx . \quad (101)$$

The air-gap permeance in front of the pole shoe equals:

$$\Lambda_g = \mu_0 \cdot \alpha_m \cdot \left(\tau \cdot \ell\right) / \left(k_C \cdot g\right) \;. \quad (102)$$

By imposing the following condition:

$$\Phi_{ps.ir} = \Phi_{ps.g} \;, \quad (103)$$

the pole shoe scalar magnetic potential is obtained:

$$U_{ps\rho d} = M_{\rho d} \cdot \frac{1}{1 + \Lambda_{ps.ir} / \Lambda_g} \cdot \frac{sin\left(\alpha_m \cdot \pi/2\right)}{\alpha_m \cdot \pi/2} \;, \quad (104)$$

from which, using (96)-(98), $b_{\rho d}(\theta_e)$ is completely defined. Its fundamental component can be calculated as:

$$B_{\rho d1} = \left(4/\pi\right) \cdot \int_0^{\pi/2} b_{\rho d}\left(\theta_e\right) \cdot cos\left(\theta_e\right) d\theta_e \;, \quad (105)$$

and the d-axis reaction coefficient equals:

$$c_d = B_{\rho d1} / B_{\rho d.is} = 0.201 \text{ (iterative result).} \quad (106)$$

B. q-axis reaction

The air-gap q-axis reaction flux density distribution is:

$$b_{\rho q}\left(\theta_e\right)=\begin{cases}B_{\rho q.is}\cdot sin\left(\theta_e\right), & 0<\theta_e<\alpha_m\,\pi/2\\ 0\ ,\ \alpha_m\dfrac{\pi}{2}<\theta_e<\theta_{e.rib}=\alpha_m\dfrac{\pi}{2}+\dfrac{p}{2}\dfrac{h_{ob}}{D_r/2} & \\ B_{\rho q.is}\cdot sin\left(\theta_e\right), & \theta_{e.rib}<\theta_e<\pi/2\end{cases}\quad . \tag{107}$$

Its fundamental component can be calculated as:

$$B_{\rho q1}=\left(4/\pi\right)\cdot\int_0^{\pi/2}b_{\rho q}\left(\theta_e\right)\cdot sin\left(\theta_e\right)d\theta_e \tag{108}$$

and the q-axis reaction coefficient equals:

$$c_q=B_{\rho q1}/B_{\rho q.is}=0.825\quad . \tag{109}$$

Thus, the unsaturated anisotropy ratio is given by:

$$\sigma_{anis.o}=c_q/c_d=4.11\ \text{(iterative result).} \tag{110}$$

C. Resistive and inductive parameters

The end-winding length can be estimated as:

$$\ell_{ew}=\left(\pi\cdot\left(D+2\cdot\left(h_{as}+h_{ts}\right)\right)/\left(3\cdot p\cdot q\right)\right)\cdot y_c\cdot\pi/2 \tag{111}$$

and the AC phase resistance can be expressed as:

$$R\left(f\right)=k_a\left(f\right)\cdot\rho_{cu.Tref}\cdot\left(U_c\cdot\left(\ell+\ell_{ew}\right)\right)/\left(a\cdot n_w\cdot A_w\right), \tag{112}$$

where $k_a(f)$ is the classical additional loss coefficient; at corner and maximum speed it is: $k_a(f_c)=1.004$; $k_a(f_M)=1.094$.

The inductive parameters are estimated as follows:

slot leakage specific permeance:

$$\lambda_{sl}=\mu_0\cdot\left(h/\left(3\cdot b_s\right)+b_1/\left(b_{as}+b_1\right)+h_{as}/b_{as}\right) \tag{113}$$

harmonic fields leak. coeff. $\sigma_h=\sigma_h\left(q,y_c\right)=1.5\cdot10^{-2}$ (114)

harm. fields leakage specific permeance: $\lambda_h=\sigma_h\cdot\lambda_{is}$ (115)

teeth tips leak. sp. perm.: $\lambda_t=\mu_0\cdot\alpha_m\cdot g/\left(b_{as}+0.8\cdot g\right)$ (116)

end-winding leakage sp. permeance: $\lambda_{ew}\approx0.3\cdot10^{-6}$ (117)

tot. leak. spec. perm.: $\lambda=\lambda_{sl}/q+\lambda_h+\lambda_t/q+\lambda_{ew}\cdot\ell/\ell_{ew}$ (118)

phase leakage inductance: $L_\ell=\left(U_c^2/p\right)\cdot\ell\cdot\lambda$ (119)

synchr. L: $L_d=L_{\rho d}+L_\ell$; $L_q\left(M_{\rho q}\right)=L_{\rho q}\left(M_{\rho q}\right)+L_\ell$ (120)

VIII. Operation Analysis, FEM Validation

In the following, the IPM motor operating quantities, both in MTPA and in Flux Weakening (FW) range are evaluated, considering winding data and quantities at the terminals:

no-load flux linkage: $\Psi_{1o}=k_w\cdot U_c\cdot\ell\cdot\phi_{g1o}/\left(2\sqrt{2}\right)$ (121)

PM flux sat. factor: $\eta_{\phi I}\left(I,\gamma\right)=\eta_\phi\left(\left(3\cdot U_c\cdot I\right)/\left(\tau\cdot p\right),\gamma\right)$ (122)

electromagnetic torque:

$$\begin{aligned}T\left(I,\gamma\right)&=T_{al}+T_{an}=\frac{3}{2}p\cdot\eta_{\phi I}\left(I,\gamma\right)\cdot\Psi_{1o}\cdot I\cdot cos\left(\gamma\right)+\\&+\frac{3}{2}p\frac{L_{\rho d}}{2}\cdot\left(\sigma_{anis.o}\cdot\sigma_{sM}\left(k_M\cdot I\cdot cos\left(\gamma\right)\right)-1\right)\cdot I^2\cdot sin\left(2\gamma\right)\end{aligned} \tag{123}$$

opt. γ angle: $\gamma_M\left(I\right)=root\left(dT\left(I,\gamma_{MG}\right)/d\gamma_{MG},\gamma_{MG}\right)$ (124)

torque in MTPA range: $T_{MTPA}\left(I\right)=T\left(I,\gamma_M\left(I\right)\right)$ (125)

corner p. I: $I_c=root\left(T_{MTPA}\left(I_{cG}\right)-T_c,I_{cG}\right)=116.0\ \text{A}_{\text{rms}}$ (126)

corner point opt. phase adv.: $\gamma_{Mc}=\gamma_M\left(I_c\right)=48.15$ deg (127)

V_d component: $$\begin{aligned}V_d\left(I,\gamma,f\right)&=-R\left(f\right)\cdot I\cdot sin\left(\gamma\right)+\\&-2\pi f\cdot L_q\left(k_M\cdot I\cdot cos\left(\gamma\right)\right)\cdot I\cdot cos\left(\gamma\right)\end{aligned} \tag{128}$$

V_q component: $$\begin{aligned}V_q\left(I,\gamma,f\right)&=2\pi f\cdot\Psi_{1o}\cdot\eta_{\phi I}\left(I,\gamma\right)+\\&+R\left(f\right)\cdot I\cdot cos\left(\gamma\right)-2\pi f\cdot L_d\cdot I\cdot sin\left(\gamma\right)\end{aligned} \tag{129}$$

phase voltage: $V\left(I,\gamma,f\right)=\sqrt{V_d^2\left(I,\gamma,f\right)+V_q^2\left(I,\gamma,f\right)}$ (130)

FW γ ang: $\gamma_{FW.I_c}\left(f\right)=root\left(V\left(I_c,\gamma_{FWG},f\right)-V_c,\gamma_{FWG}\right)$ (131)

γ in all the range: $$\gamma\left(f\right)=\begin{cases}\gamma_{Mc} & 0<f<f_c\\ \gamma_{FW.I_c}\left(f\right) & f_c<f<f_M\end{cases} \tag{132}$$

Fig.13 shows the transient FEM simulation of the electromagnetic torque, corresponding to the operating condition of the corner point; the following remarks arise:

- the average torque is very close to the corner point torque ($T_{avg}/T_c=0.9996$); this shows the sizing method goodness;
- the peak-peak torque ripple equals 3.48%, that confirms the good initial choice of $q=5/2$ slots/(pole·phase).
- Fig. 14 shows the phase advance as a function of speed, calculated analytically by (132).

For $0<N<N_M$, with $I=I_c$, and by (123), (130), (132), the torque and voltage analytical curves follow, shown in fig. 15, together with the corresponding FEM calculated values (for N = 1, 2, 2.9, 3, 4, 5, 6, 7, 8, 9, 10, 11, 12, 13, 13.5 kRPM).

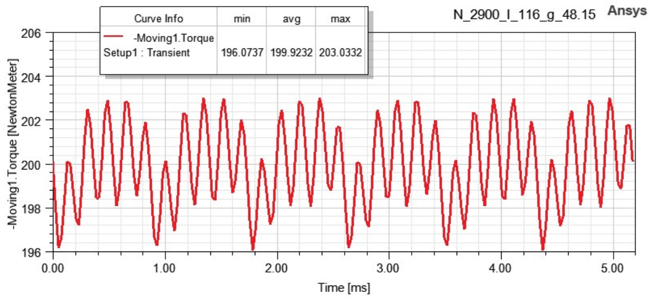

Fig. 13. Torque waveform in the base point, from FEM transient simulation.

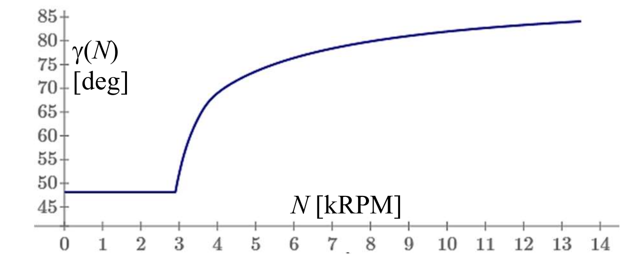

Fig. 14. Phase advance as a function of speed, calculated by (132).

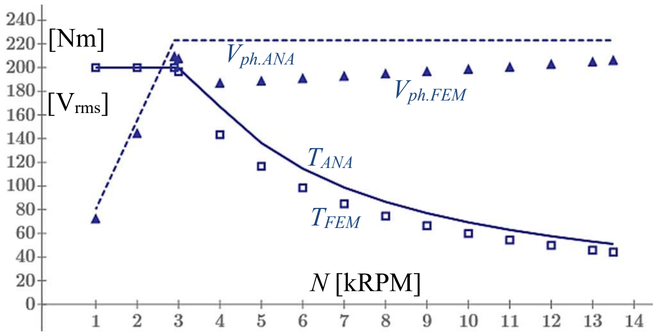

Fig. 15. Torque and voltage, calculated analytically by (123) (—) and (130) (---) and by FEM (points □ and ▲), using phase advance (132).

As can be observed, while the agreement in MPTA range ($N < N_c = 2.9$ kRPM) is good, a significant discrepancy occurs in FW range; the reasons for this behavior are:

- in MTPA range, the imposed condition is $T = T_c$, by (126); in FW range the condition is $V = V_c$, by (131), that suffers of a lower parameter accuracy in V estimation, by (130);
- the sensitivity of torque and speed on the angle γ, low in the MTPA range, increases significantly with the increase of speed above $N_c = 2900$ RPM, as shown in fig. 16.

Fig. 17 shows again the γ curve calculated analytically (γ_{ANA}), together with a γ curve calculated by FEM (γ_{FEM}): each point of the γ_{FEM} curve has been chosen in such a way to obtain the same torque calculated analytically (by (123), with $I = I_c$ and γ from (132)): by inserting the γ_{FEM} values in (130), more congruent V values follow, as can be seen in fig. 18.

IX. Conclusion

A model of the IPM motor has been developed, oriented to design, considering saturation and cross-coupling effects.

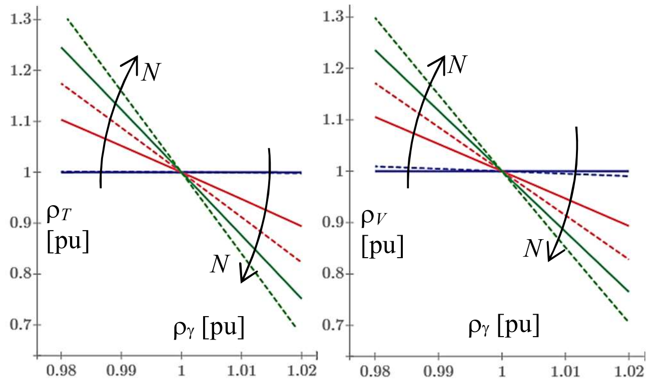

Fig. 16. Sensitivity of pu torque and pu voltage as a function of γ change (up to ±0.02 pu, with respect to γ from (132)); $N = 0, 3, 6, 9, 12, 15$ kRPM.

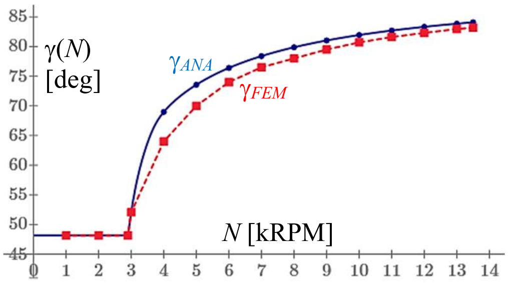

Fig. 17. Phase advance as a function of speed: $\gamma_{ANA}(N)$ = calculated analytically by (132); $\gamma_{FEM}(N)$ = calculated by FEM (in such a way to obtain, for each point, a torque equal to that calculated analytically).

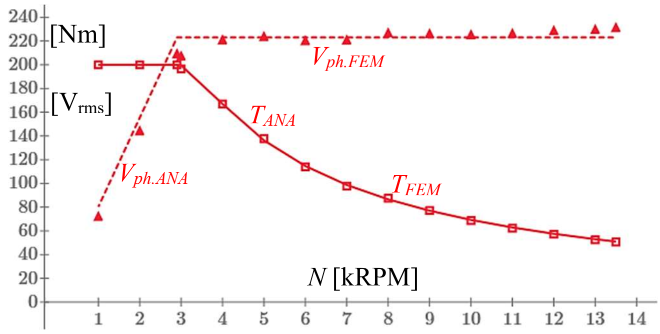

Fig. 18. Torque and voltage, calculated analytically by (132) and numerically by FEM, using phase advance γ_{FEM} of fig. 17.

A sizing equation has been obtained, not dependent on winding data and useful to guide the sizing procedure: this approach not only is quicker compared with FEM, but it gives an insight into the motor electromagnetic behavior.

Comparison with FEM calculations have shown very good agreement in the corner point and in MTPA range, while some inaccuracies arise in FW range, mainly due to imperfect estimation of the phase advance.

X. References

[1] L. Zhu, S. Z. Jiang, Z. Q. Zhu and C. C. Chan, "Analytical Modeling of Open-Circuit Air-Gap Field Distributions in Multisegment and Multilayer IPM Machines," in IEEE Trans. on Mag., vol. 45, no. 8, pp. 3121-3130, Aug. 2009.

[2] K. Kamiev, J. Montonen, M. P. Ragavendra, J. Pyrhönen, J. A. Tapia, and M. Niemelä, “Design principles of PM synchronous machines for parallel hybrid or traction applications,” IEEE Trans. Ind. Electronics, vol. 60, no. 11, pp. 4881-4890, Nov. 2013.

[3] W.-H. Kim, M.-J. Kim, K.-D. Lee, J.-J. Lee, J.-H. Han, T.-C. Jeong, S.-Y. Cho, J. Lee, “Inductance calculation in IPMSM considering magnetic saturation,” IEEE Trans. Mag., vol. 50, no. 1, Jan. 2014.

[4] H. Chen, D. Li, R. Qu, Z. Zhu, and J. Li, “An improved analytical model for inductance calculation of IPM machines,” IEEE Trans. Mag., vol. 50, no. 6, Jun. 2014, Art. no. 7027108.

[5] X. Chen, J. Wang, B. Sen, P. Lazari, and T. Sun, “A High-Fidelity and Computationally Efficient Model for IPM Machines Considering the Magnetic Saturation, Spatial Harmonics, and Iron Loss Effect,” IEEE Tran. on Ind. Electronics, v. 62, no. 7, pp. 4044-4055, Jul. 2015.

[6] G. Xu, G. Liu, S. Jiang, and Q. Chen, “Analysis of a hybrid rotor permanent magnet motor based on equivalent magnetic network,” IEEE Trans. Mag., vol. 54, no. 4, Apr. 2018, Art. no. 8202109.

[7] A. Di Gerlando, G. M. Foglia and R. Perini, "Procedure to Define an Accurate Model for Saturation and Cross-Coupling in IPM Machines," Intern. Conf. on Electr. Machines (ICEM), 2020, pp. 291-297.

[8] S. Wu, T. Shi, L. Guo, H. Wang and C. Xia, "Accurate Analytical Method for Magnetic Field Calculation of IPM Motors," IEEE Trans. on Energy Conversion, vol. 36, no. 1, pp. 325-337, March 2021.

[9] E. Armando, P. Guglielmi, G. Pellegrino, M. Pastorelli, and A. Vagati, “Accurate Modeling and Performance Analysis of IPM-PMASR Motors,” IEEE Trans. on Ind. Appl., v.45, no.1, pp.123-130, Jan. 2009.

[10] N. Bianchi, D. Durello, and E. Fornasiero, “Multi-objective optimization of an Interior PM motor for a high-performance drive,” XXth Int. Conf. on Electr. Machines (ICEM), Sep. 2012, pp. 378-384.

[11] Chunting Mi, M. Filippa, Weiguo Liu and Ruiqing Ma, "Analytical method for predicting the air-gap flux of interior-type PM machines," in IEEE Trans. on Mag., vol. 40, no. 1, pp. 50-58, Jan. 2004.

[12] R. Rocca, F. Giulii Capponi, G. De Donato, S. Papadopoulos, F. Caricchi, M. Rashed, M. Galea, "Actual Design Space Methodology for Preliminary Design Analysis of Switched Reluctance Machines," IEEE Trans. on Ind. Appl., vol. 57, no. 1, pp. 397-408, Jan.-Feb. 2021.

[13] S. Huang, J. Luo, F. Leonardi, T. A. Lipo, "A general approach to sizing and power density equations for comparison of electrical machines," IEEE Trans. Ind. Appl., v.34, no.1, pp.92-97, Jan. 1998.

[14] F. Parasiliti, M. Villani, S. Lucidi, and F. Rinaldi, “Finite-Element-Based Multiobjective Design Optimization Procedure of IPM Synchronous Motors for Wide Constant-Power Region Operation,” IEEE Trans. on Ind. Electr., vol. 59, no. 6, pp. 2503-2514, Jun. 2012.

XI. Biographies

Antonino Di Gerlando (M’92-SM’17) received his MS degree in electrical engineering from the Politecnico di Milano, Italy, in 1981. Currently, he is a Full Professor at the Department of Energy at Politecnico di Milano. Fields of interest: design and modeling of electrical machines, converters, and drive systems. He is a senior member of IEEE and a member of the Italian Association of the Electric and Electronic Engineers (AEI).

Claudio Ricca received the M.S. degree in electrical engineering from Politecnico di Milano, Italy, in 2017. He is currently a PhD student at Politecnico di Milano. Fields of interest: design and modeling of electrical machines and drives.